



## Efficient photocatalytic overall water splitting over a core-shell GaInZnON@GaInON homojunction

Wenlong Fu<sup>a</sup>, Xiangjiu Guan<sup>a</sup>, Zhenxiong Huang<sup>a</sup>, Maochang Liu<sup>a,b,\*</sup>, Liejin Guo<sup>a,b,\*</sup>

<sup>a</sup> International Research Center for Renewable Energy, State Key Laboratory of Multiphase Flow in Power Engineering, Xi'an Jiaotong University, 28 No. Xianning West Road, Xi'an, Shaanxi 710049, PR China

<sup>b</sup> Suzhou Academy of Xi'an Jiaotong University, 99 No. Renai Road, Suzhou, Jiangsu 215123, PR China



### ARTICLE INFO

**Keywords:**  
Photocatalysis  
Overall water splitting  
Oxynitride  
Core-Shell structure

### ABSTRACT

Direct overall water splitting *via* photocatalysis provides a potential pathway for solar energy conversion. The essential section is to develop efficient and stable photocatalysts, yet with limited success to date. Here a novel *p*-type gallium indium zinc oxynitride homojunction photocatalyst with core-shell structure is reported, which exhibits H<sub>2</sub> and O<sub>2</sub> evolution rates of 603 and 274 μmol h<sup>-1</sup> g<sup>-1</sup> with an apparent quantum efficiency of 3.5% at 430 nm from overall pure water splitting. Precise characterizations and DFT calculations reveal that the excellent photocatalytic performance is ascribed to the facilitated charge transfer contributed by the ideal type-I band alignment between GaInZnON core and GaInON shell, combined with the intermediate level formed nearby the Fermi level of GaInON shell. Our work offers insight into the development of facile synthesis of core-shell structure photocatalysts towards efficient solar-driven overall water splitting.

### 1. Introduction

Photocatalytic water splitting into H<sub>2</sub> and O<sub>2</sub> is an appealing approach for clean and renewable energy. Since the first report of photo-induced water splitting by TiO<sub>2</sub> electrodes back in 1972 [1], extensive studies have been conducted to develop versatile photocatalysts that can split water *via* solar irradiation [2–7]. To date, numerous photocatalysts, such as Cd<sub>x</sub>Zn<sub>1-x</sub>S, SrTiO<sub>3</sub>, graphitic carbon nitride (g-C<sub>3</sub>N<sub>4</sub>), WO<sub>3</sub>, BiVO<sub>4</sub>, and TaON, have been identified to efficiently generate either H<sub>2</sub> or O<sub>2</sub> in the presence of sacrificial agents under visible-light irradiation [8–13]. Although these photocatalysts have made a great success in half-cell photocatalytic performance, efficient visible-light driven overall water splitting with stoichiometric H<sub>2</sub> and O<sub>2</sub> evolution still remains a challenge.

Of the very limited photocatalysts that were reported to be capable of overall water splitting under visible-light irradiation, nitride/oxynitride drew preferential attention. This preference stems from their tunable composition/structure for visible light response and relatively high stability toward photocorrosion. Notable examples include GaN:ZnO solid solution [14], Ta<sub>3</sub>N<sub>5</sub> nanorods/cuboid KTaO<sub>3</sub> hybrids [15], LaMg<sub>x</sub>Ta<sub>1-x</sub>O<sub>1+3x</sub>N<sub>2-3x</sub> [16], C<sub>3</sub>N<sub>4</sub> [17], and InGaN [18]. These photocatalysts have shown good capability for visible-light-driven overall water splitting. Despite these successful demonstrations, it is still worth noting that such abilities highly relied on incorporation of

cocatalytic materials such as carbon q-dots or Cr<sub>2</sub>O<sub>3</sub>/Rh. These cocatalysts were, however, synthetically complex or even irreproducible. On the other hand, for a given photocatalyst, the photocatalytic property also depends on its microstructure. As was widely reported, core-shell nanostructure usually represents a versatile design platform for superior energy-conversion properties through the as-established heterostructure when compared with their bulk counterparts [19–24]. This superiority can be explained by the finely divided electronic states for promoted charge separation and surface reaction involved in the tunable core and shell component. However, due to the lack of available overall-water-splitting photocatalyst and limited synthetic methods for particulate photocatalyst, overall water splitting, to the best of our knowledge, has not yet been realized on a core-shell particulate photocatalyst.

In this work, we report a novel ternary-gallium zinc indium oxynitride (GIZON) with core-shell structure for one-step-excitation overall water splitting. The success to synthesis relies on the controlled diffusion of In and Zn ions involved the crystallization process that is induced by the difference of evaporation rate and lattice mismatch. The relationship between In-GZON core and GION shell was comprehensively analyzed by systematic characterization combined with theoretical calculations, and the unique type-I heterostructure formed by core and shell was found to benefit charge separation and to boost the efficiency of overall water splitting under visible light irradiation.

\* Corresponding author at:

E-mail addresses: [maochangliu@mail.xjtu.edu.cn](mailto:maochangliu@mail.xjtu.edu.cn) (M. Liu), [lj-guo@mail.xjtu.edu.cn](mailto:lj-guo@mail.xjtu.edu.cn) (L. Guo).

## 2. Experimental method

### 2.1. Synthesis

Typical preparation processes of photocatalysts were shown in Fig S1. Gallium nitrate hydrate ( $\text{Ga}(\text{NO}_3)_3 \cdot x\text{H}_2\text{O}$ , 1.25 mmol), indium nitrate hydrate ( $\text{In}(\text{NO}_3)_3 \cdot x\text{H}_2\text{O}$ , 1.25 mmol), and zinc acetate dihydrate ( $\text{Zn}(\text{Ac})_2 \cdot 2\text{H}_2\text{O}$ , 2.5 mmol) were dissolved in mixed solution of ethanolamine (MEA,  $\text{HOCH}_2\text{CH}_2\text{NH}_2$ , 4 mL) and acetic acid ( $\text{CH}_3\text{COOH}$ , 0.1 mL). The as-obtained Ga-In-Zn (GIZ) solution was then stirred at 65 °C for 2 h, followed by one-week aging at 0 ~ 2 °C. Afterwards, the resulting gel-like GIZ precursor was calcined at 500 °C for 10 h with a heating rate of 3 °C/min. The as-obtained light-yellow fluffy powder was collected and designated as GIZO. Ultimately, GIZO powder was nitrated with ammonia (200 sccm) at 850 °C for 10 h with a heating rate of 5 °C/min and cooling rate of 3 °C/min. The as-obtained dark-gray floppy powder was designated as GIZON. For comparison, sample without Zn precursors was prepared and designated as GION.

### 2.2. Photocatalytic reaction

Photocatalytic water splitting was conducted in a gas-closed system with a side irradiation Pyrex cell. Photocatalyst powder (30 mg) was dispersed and mixed with a certain amount of cocatalyst precursor in deionized water (40 mL) under continuous magnetic stirring. All cocatalysts (1 wt %) were loaded on the GIZON via the photodeposition method. After evacuated by Ar gas for over 20 min., the reaction suspension was irradiated by visible light from a 300 W Xe lamp equipped with a 420-nm cutoff filter. The amount of evolved  $\text{H}_2$  and  $\text{O}_2$  was determined using a gas chromatograph (Presee-G5).

For AQY, photocatalyst powder (50 mg) was dispersed and mixed Rh (1 wt%) in deionized water (40 mL) using 430 nm band-pass filters. The hydrogen rate was measured by the amount of  $\text{H}_2$  determined by a gas chromatograph in a certain time, for example 2 h. After that, the light intensity around the photocatalytic cell position using 430 nm was measured by the irradiation meter. Then the number of incident photons was defined by the following equation:

$$N_p = PS\lambda/hc$$

where  $P$  is the light intensity was measured by the irradiation meter;  $S$  is the area of the light acceptance;  $\lambda$  is the wavelength of the illumination;  $h$  is the Plank constant  $\sim 6.626 \times 10^{-34}$  J·s and  $c$  is the speed of light  $\sim 3 \times 10^8$  m/s. Apparent quantum yield (AQY) was defined by the following equation:

$$AQY = 2N_H/N_p \quad (1)$$

where  $N_H$  is the number of evolved  $\text{H}_2$  molecules and  $N_p$  is the number of incident photons.

The turnover number (TON) in terms of GIZON in the photocatalysts was calculated according to the following equation:

TON = the number of reacted electrons/the number of GIZON in the photocatalyst

The TON in terms of GIZON in the photocatalysts was calculated by evaluating the water splitting for 5 h using 30 mg of photocatalyst.

### 2.3. Characterization

The crystallite morphologic micrographs were obtained from a JEOL JSM-7800 F field-emission scanning electron microscopy (SEM), and an FEI Tecnai F30 transmission electron microscopy (TEM). Elemental mapping over the selected region of the photocatalyst was conducted by an energy-dispersive X-ray spectrometer (EDX) attached to the FEI Tecnai F30 TEM. Chemical states of the samples were obtained from an AXIS Ultra DLD X-ray photoelectron spectroscopy (XPS) developed by Shimadzu/Kratos Analytical, Japan. X-ray diffraction

(XRD) measurements were performed on an X'Pert PRO diffractometer with  $\text{Cu K}\alpha$  irradiation ( $\lambda = 1.5438 \text{ \AA}$ ) and scanning. All the samples were scanned step size of 0.03° between 20° and 80°. The UV-vis absorption spectra of the samples were collected from a Hitachi U-4100 UV-vis-near-IR spectrophotometer. Photoluminescence (PL) emission spectra were obtained on a PTI QM-4 fluorescence spectrophotometer at room temperature using an excitation wavelength of 325 nm.

### 2.4. Electrochemical measurements

Mott-schottky plots were performed in a three-electrode system with an electrochemical station (CHI 700D), which was conducted in 0.5 M  $\text{Na}_2\text{SO}_4$  electrolyte using  $\text{Ag}/\text{AgCl}$  electrode as the reference electrode, Pt as the counter electrode, and the glassy carbon electrode covered with samples as working electrode, respectively. Before measuring, the electrolyte was purged with  $\text{N}_2$  for 30 min to remove the oxygen in the electrolyte. The tests were carried out at a frequency of 1 kHz in a potential range of 1.2–2.5 V (vs. RHE) under dark condition.

Prior to the Mott-Schottky experiments, these GIZO and GIZON films were prepared by doctor blade method, and the pastes were consisted of samples powder, deionized water, ethanol and nafion solution. Moreover, the flat band potential of semiconductor film in a liquid junction can be estimated from the Mott-Schottky equation

$$C_{sc}^{-2} = (2/\epsilon\epsilon_0 N_D)(E - E_{fb} - \kappa T/e) \quad (2)$$

where  $C_{sc}$  is the space charge capacitance in  $\text{F cm}^{-2}$ ;  $e$  is the electronic charge in C;  $\epsilon$  is the dielectric constant of the semiconductor;  $\epsilon_0$  is the permittivity of free space;  $N_D$  is the carrier density in  $\text{cm}^{-3}$ ;  $E$  is the applied potential in V;  $E_{fb}$  is the flat band potential in V;  $\kappa$  is the Boltzmann constant; and  $T$  represents the temperature in K. The temperature related term ( $kT/e$ ) in Eq. 2 is negligible, 0.0257, at room temperature. The flat band potential is obtained from the x-intercept of the tangent line of the Mott-Schottky (M-S) plot on potential axis.

### 2.5. Calculation Details of the spacing of Moire' fringes

The spacing of Moire' fringes were calculated using the following expression:

$$M = m_2 m_1 / (m_2 - m_1) \quad (3)$$

where  $M$  is the spacing of two stripes, and  $m_1$  and  $m_2$  are the crystalline-lattice mismatch of the overlapping {4-2-20} planes of core and shell, respectively. In our case, given  $m_1 = 0.138 \text{ nm}$  and  $m_2 = 0.149 \text{ nm}$ ,  $M = 1.869 \text{ nm}$  was obtained [25].

## 3. Results and discussion

Based on the experiment process, the plausible mechanisms for the evolution pathways and the growth mode are schematically illustrated in Fig. 1. Firstly, metal precursors dispersed in the MEA formed a uniform gel-mixture through heat and longtime preservation at a relative low temperature. During calcination in air, organics (mainly MEA) turned into gas production (vapor,  $\text{CO}_2$  and  $\text{NH}_3$ , green balls in Fig. 1a) inside-out along the blue crooked arrows  $d_1$ , which incises the whole colloid into GIZO nanoparticles with a small size (yellow particles in Fig. 1b). As was depicted in the dashed box of Fig. 1b, the small GIZO nanoparticle was homogeneously composited with Ga, Zn, and In elements.

When treated with  $\text{NH}_3$  for nitridation, the as-formed GIZON tended to present a core-shell structure (see later characterization results), which was resulted from the different volatilization rate of Zn and In elements (Fig. 1b) [26–29]. In detail, due to smaller mismatch of Zn and Ga compared to that of In and Ga, Ga preferred to form solid solution with Zn, namely  $\text{GaN@ZnO}$  (GZON), leading to a relatively faster rate of In volatilization. Meanwhile, GZON solid solution with more stable

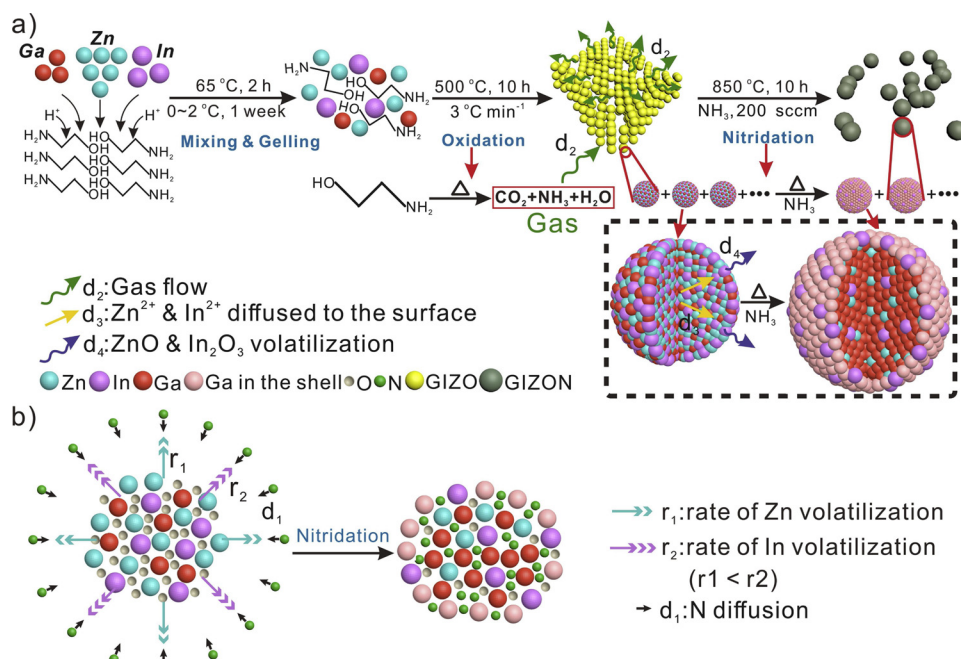


Fig. 1. Schematic illustration of major steps involved in the growth process of GIZON.

formation also restricted the formation of GaInON solid solution by pushing In component to the outer layer of the nanoparticles. In addition, due to Zn volatilization, most of the In element survives in Zn vacancy distributed in the surface region, forming a Ga-In composite shell (GION).

To investigate the entire reaction process, the structure and

composition of as-prepared GIZON nanocrystals were analyzed with several characterizations, and the results are shown in Fig. 2. TEM image in Fig. 2a presented the GIZON nanocrystals composed of small particles. The particle size under 10 nm (marked by the red dashed frame) and interplanar spacing of 2.78 Å were revealed in high-magnification TEM image of Fig. 2b. The corresponding electron diffraction

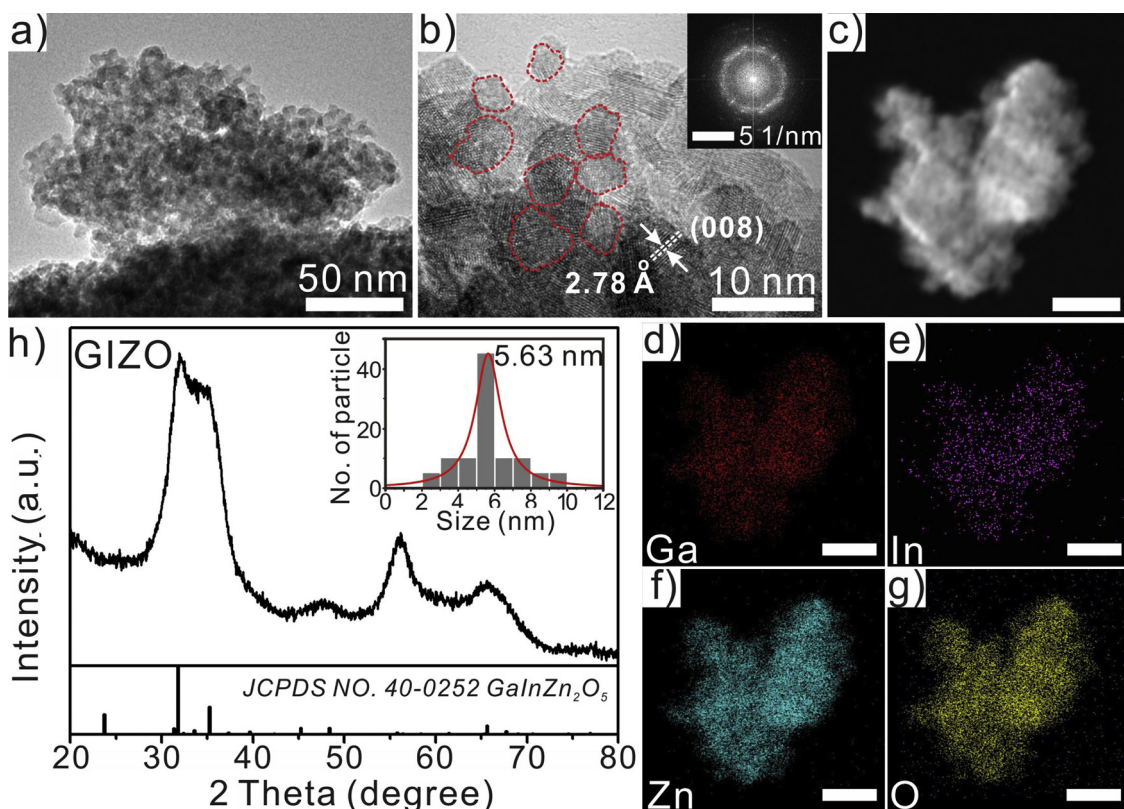
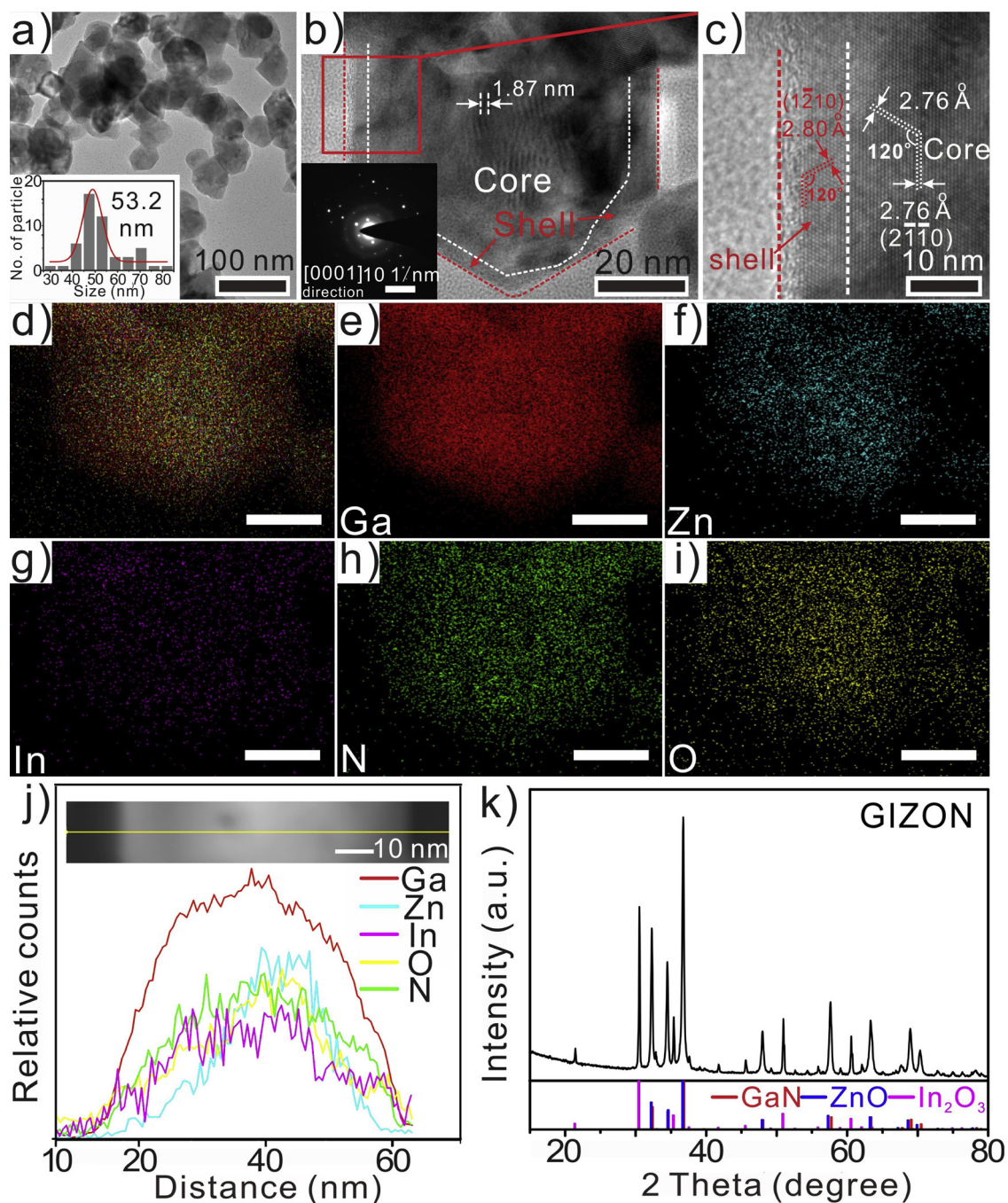


Fig. 2. (a) Low-magnification and (b) High-resolution TEM images of GIZON nanoparticles with the inset image corresponding to the electron diffraction patterns. (c-g) EDX mapping images showing the corresponding elemental distribution in GIZON. Scale bars in the images are 100 nm. (h) XRD patterns of GIZON, as well as the size distribution shown in the inset image.



**Fig. 3.** (a) Low- and (b) High-magnification TEM images of GIZON nanoparticles; the inset images correspond to size distribution and electron diffraction patterns, respectively. (c) High-resolution TEM images of GIZON viewed from [0001] direction corresponding to the area marked by the red box in the (b). (d–i) EDX mapping images showing the corresponding elemental distribution in a single GIZON nanocrystal. Scale bars in the images are 20 nm. (j) EDX line scan and (k) XRD patterns of GIZON (For interpretation of the references to colour in this figure legend, the reader is referred to the web version of this article).

patterns in the inset image indicated the polycrystalline nature. Besides, EDX mapping images (Fig. 2, c–g) demonstrated homogeneous distributions of Ga, Zn, In, and O, indicating the solid solution feature of as-prepared GIZO nanocrystals. Except the EDS spectra shown in Fig S3a, Fig. 2h showed good accordance between XRD patterns of as-prepared GIZO nanocrystals and standard  $\text{GaInZn}_2\text{O}_5$  (JCPDS NO. 40-0252), which also agrees well with the ratio of metal precursors during the preparation process. Based on the Scherrer's formula, the broad Bragg peaks also manifested small grain size of GIZO crystals, which was also confirmed by the size distribution statistics as shown in the inset image (average size: 5.63 nm). Thus, a large specific surface area of GIZO was also obtained shown in Fig S4a.

GIZON was obtained by nitridation treatment of afore-synthesized GIZO, and was comprehensively analyzed from the morphology, component, and structure aspects. Fig. 3a presents the TEM images of GIZON particles. They were characterized by an average size of 53.2 nm, which also leads to a relative small specific surface area (Fig S4b). Fig. 3b shows SAED pattern from [0001] view, implying the typical hexagonal structure. It is worth noting that a unique core-shell structure could be revealed from HRTEM as shown in Fig. 3c (red rectangle area in Fig. 3b), with lattice fringes of 2.76 and 2.80 Å for core and shell, respectively. The viewpoint was further validated by elemental EDX mapping images as shown in Fig. 3, d–i. Clearly, Zn (Fig. 3f) distributed mainly in the core region (labeled by white dash

line in Fig. 3b) of GIZON nanoparticles, which was further confirmed by EDX line scan (Fig. 3j). Meanwhile, compared with other elements shown in Fig S3b, In content was relatively less, which also validated the vaporization phenomena. Thus, the core was designated as In-GZON. More importantly, based on the theoretical model of GIZON and line scan of In element shown in the Fig S2, the concentration of In between core and shell is close to the ratio of 1: 2, indicating that In mainly existed in shell.

Fig. 3k presents the XRD spectrum of GIZON nanocrystals. It could be seen that some of the diffraction peaks shifted to lower angles compared to those of GaN (JCPDS NO.76-0703,  $a = b = 3.19 \text{ \AA}$ ,  $c = 5.189 \text{ \AA}$ ) but higher angles than those of ZnO (JCPDS NO.75-1526,  $a = b = 3.22 \text{ \AA}$ ,  $c = 5.20 \text{ \AA}$ ), indicating the formation of a solid solution rather than simple mixture of GaN and ZnO [30]. The rest peaks shifted to lower angles with respect to those of  $\text{In}_2\text{O}_3$ . Therefore, the shell was designated as GION. Consequently, the as-prepared GIZON nanocrystals were composed with In-GZON core and GION shell. Furthermore, the lattice mismatch between In-GZON core and GION shell reaches 14.5% (lattice constants of 2.76 vs 2.80  $\text{\AA}$ , respectively), which could result in strong interfacial strain and thus slight lattice disorder near the interface of the core-shell structure. It can also lead to the Moire patterns with a fringe distance of about 1.87 nm shown in Fig. 3b, which corresponded to the d-spacing difference overlapped {200} planes of In-GZON and GION and further demonstrated the formation of core-shell structure [31]. Gradually, moire patterns have been a potent proof of different composites.

We next sought to investigate the optical property of the as-prepared particles. Fig. 4a presents the UV-vis spectra of the as-prepared GIZO and GIZON with sharp absorption edge, indicating better light-absorption of GIZON in visible-light range compared with GIZO. Correspondingly, the band gap of GIZO and GIZON was determined as 2.74 and 2.51 eV from Tauc plots depicted in Fig. 4b, demonstrating band structure modification attributed to N incorporation. Photoluminescence (PL) spectra for both GIZO and GIZON nanocrystals were measured and are shown in Fig. 5. Based on the UV-vis spectrum, the peaks exhibited a little blue shift compared to the band gap energy. As was reported that the increase of In could reduce the band gap of GaN base semiconductor, this phenomenon may be caused by the emission from the poor In are (the core In-GZON). The PL intensity of GIZON shows a higher state than that of GIZO, suggesting the larger size and more capture sites in GIZON nanocrystals, such as core-shell interfaces, crystallize boundaries, defects, and the like. Interestingly, there is a gradual peak at the ~620 nm, which should be derived from the bond of In-N consisting in the shell GION [32], which is also verified by the XPS spectra shown in Fig S5c. Except that, Fig S7 also indicates GIZO and GIZON are the p-type semiconductor.

Photocatalytic performance for overall water splitting under visible-light irradiation was then evaluated. Fig. 6a shows gas production rates of GIZON photocatalyst modified with various metals (Pt, Rh, Ru, Ag, Au, Ni, and Cr, 1 wt %) as cocatalyst. Outstanding  $\text{H}_2$  ( $603 \mu\text{mol h}^{-1} \text{g}^{-1}$ ) and  $\text{O}_2$  ( $274 \mu\text{mol h}^{-1} \text{g}^{-1}$ ) production was observed when Rh was loaded, with the stoichiometric ratio of  $\text{H}_2$  and  $\text{O}_2$  (~2:1). TON

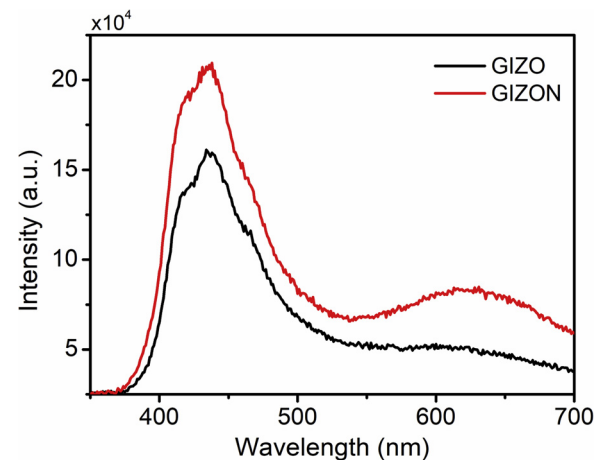


Fig. 5. Photoluminescence spectra of GIZO and GIZON under 337 nm excitation at room temperature.

values of 1.71 were obtained for GIZNO nanocrystals, meaning that this reaction is a photocatalytic process instead of a photochemical reaction. The corresponding apparent quantum yield (AQY) was determined to be 3.5% at 430 nm, which is among the best numbers reported on oxynitride photocatalysts. Besides, water splitting activity was optimized by investigating different amount of Rh loaded as shown in Fig. 6b, and long-term performance in Fig S6 demonstrated the excellent stability on this unique core-shell structured ternary oxynitride.

In order to get a clear illustration of this unique core-shell oxynitride, band structures were investigated by calculating the density of states (DOS) and partial density of states (PDOS) for In-GZON (core) and GION (shell), as presented in Fig. 7. For In-GZON (Fig. 7a), the conduction band minimum (CBM) was mainly consisted of Ga-3s and Ga-3p state, while the valence band was significant contributed by O-2p and N-2p states, with very small contributions from Zn-3d, In-5s and In-5p states that formed the valence band maximum (VBM). For GION (Fig. 7b), the valence band (VB) was also mainly derived from O-2p and N-2p states with a small contribution of the In-5s, In-5p, Ga-3s and Ga-3d states. Interestingly, a few intermediate levels originated from In was found nearby the Fermi level, which was similar to what has been reported by Dou et al [33].

Possible mechanism of photocatalytic overall water splitting on GIZON core-shell nanocrystals was illustrated in Fig. 8, which could be ascribed to the following aspects: on one hand, the band-edge potential of CB and VB, designated as  $E_{\text{CB}}$  and  $E_{\text{VB}}$ , could be calculated from the following equation:

$$E_{\text{CB}} = \chi - E_0 - 1/2 E_g \quad (4)$$

$$E_{\text{VB}} = E_{\text{CB}} + E_g \quad (5)$$

where  $\chi$  is the absolute electronegativity of the semiconductor, determined by the geometric mean of the absolute electronegativity of

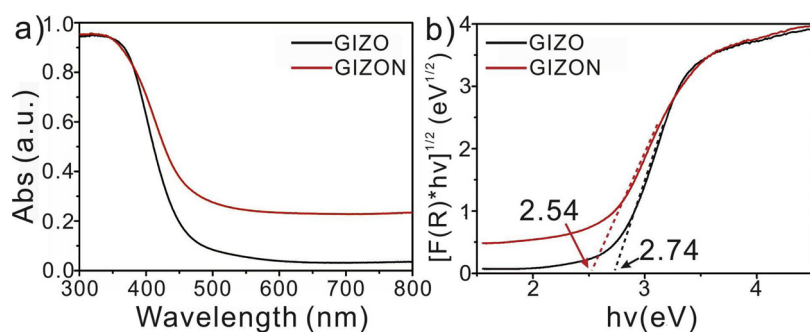


Fig. 4. (a) UV-vis absorbance spectra and (b) the corresponding Tauc plots of GIZO and GIZON.

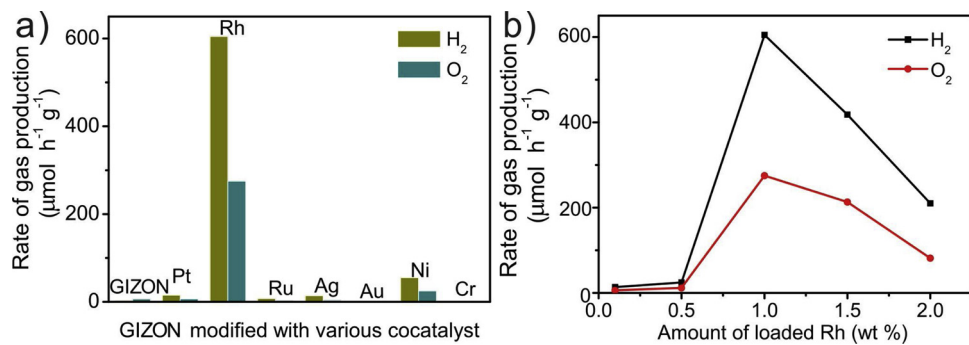


Fig. 6. (a) Photocatalytic activity of GIZON modified with various transition metals for overall water splitting (b) Dependence of overall water splitting activity of GIZON on various Rh loading amounts. Reaction conditions: 30 mg catalyst, 40 mL H<sub>2</sub>O, 300 W Xe lamp ( $\lambda > 420$  nm), Reaction time is 5 h for the average rate.

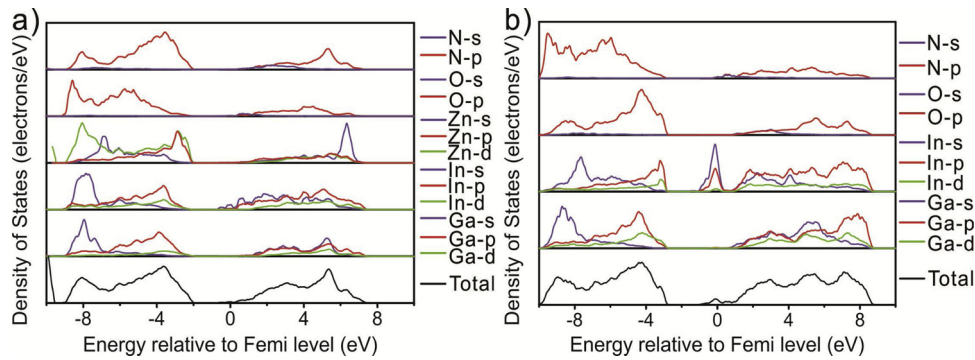


Fig. 7. The DOS and PDOS of (a) In-GZON core and (b) GION shell, respectively.

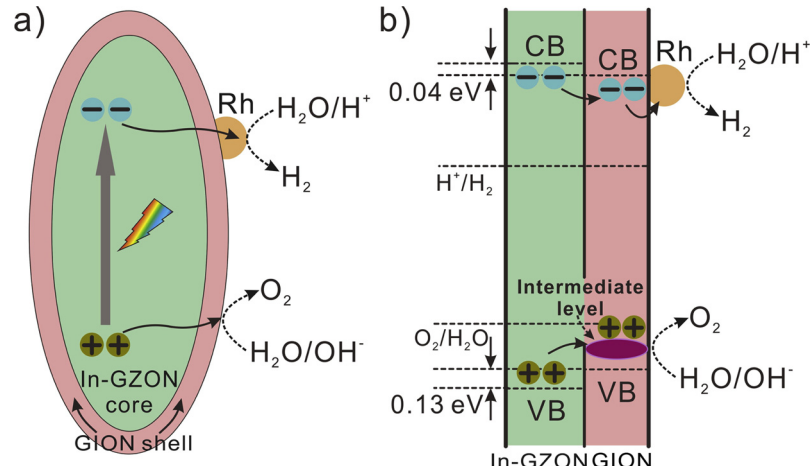


Fig. 8. Proposed mechanism for the GIZON photocatalytic reaction system.

constituent atoms, *i.e.*, the arithmetic mean of the atomic electron affinity and the first ionization energy;  $E_0$  is the energy of free electrons on the hydrogen scale; and  $E_g$  is the band gap of the semiconductor [34], which was shown in both Fig. 4 and Fig S8.  $E_{CB}$  and  $E_{VB}$  of In-GZON core were determined to be  $-0.86$  and  $1.68$  eV, while those of GION shell were  $-0.82$  and  $1.55$  eV. Thus, the  $E_{CB}$  and  $E_{VB}$  of In-GZON core were  $-0.04$  eV and  $0.13$  eV relative to that of In-GION. Except that, the Based on the band energy alignment, an illustration of possible interface electron transfer behavior between the core and shell was proposed. When excited under visible-light irradiation, electrons from CBM of In-GZON core would be immigrated to the less negative CBM of GION shell, and then to Rh co-catalyst for the reduction process of H<sup>+</sup> to H<sub>2</sub> [35]; As for oxygen evolution reaction, based on the analysis of DOS and PDOS combined with p-type character of GION, there was an intermediate level close to the VBM of GION shell, which is less positive

than that of In-GZON core. Thus, photoexcited holes from VBM of In-GZON core would be transferred to the less positive intermediate level of GION shell and oxidized H<sub>2</sub>O to evolve O<sub>2</sub>. This type-I heterostructure would accelerate the transfer of photogenerated electrons/holes from core to the shell, hence boost the efficiency for photocatalytic overall water splitting which was further supported by significant different photocatalytic activity between GaZnON (GZON) and GIZON with core-shell structure (Fig S9).

#### 4. Conclusion

In summary, a p-type ternary-gallium zinc indium oxynitride (GIZON) was successfully prepared *via* nitridation assisted sol-gel method. It was verified that the as-prepared GIZON was consisted of core-shell structure with the core of In-doped GaN@ZnO (In-GZON)

solid solution and the shell of  $\text{GaN@In}_2\text{O}_3$  (GION) composite. This unique core-shell composition constructed an ideal type-I band alignment for efficient charge separation. Significantly, In intermediate level formed near the Fermi level in GION shell, as was revealed by DFT calculation, further facilitated hole transfer in as-prepared composited photocatalyst. Consequently,  $\text{H}_2$  and  $\text{O}_2$  production of  $603 \mu\text{mol h}^{-1} \text{g}^{-1}$  and  $274 \mu\text{mol h}^{-1} \text{g}^{-1}$ , with an AQY of 3.5% at 430 nm was achieved for unassisted visible-light driven overall water splitting without any sacrificial agents. Our work presents not only a facile method for the synthesis core-shell structure nanomaterials, but also insights and guidance on the development of efficient and stable photocatalysts for one-step-excitation overall water splitting.

### Competing financial interests

The authors declare no competing financial interests

### Acknowledgement

W. F. and X. G. contributed equally to this work. This work is supported by the Basic Science Center Program for Ordered Energy Conversion of the National Natural Science Foundation of China (No. 51888103), the National Natural Science Foundation of China (No. 51876173), the Shaanxi Technical Innovation Guidance Project (No. 2018HJCG-14), and China Fundamental Research Funds for the Central Universities.

### Appendix A. Supplementary data

Supplementary material related to this article can be found, in the online version, at doi:<https://doi.org/10.1016/j.apcata.2019.05.043>.

### References

- [1] A. Fujishima, K. Honda, *Nature* 238 (1972) 37–38.
- [2] K. Mori, H. Kakudo, Yamashita H, *ACS Catal.* 4 (2014) 4129–4135.
- [3] J. Quinn, J. Hemmerling, S. Linic, *ACS Catal.* 8 (2018) 8545–8552.
- [4] R. Shi, Y.H. Cao, Y.J. Bao, Y.F. Zhao, G.I.N. Waterhouse, Z.Y. Fang, L.Z. Wu, C.H. Tung, Y.D. Yin, T.R. Zhang, *Adv. Mater.* 29 (2017) 1700803.
- [5] H.J. Yu, R. Shi, Y.X. Zhao, T. Bian, Y.F. Zhao, C. Zhou, G.I.N. Waterhouse, L.Z. Wu, C.H. Tung, T. R. Zhang, *Adv. Mater.* 29 (2017) 1605148.
- [6] C. Zhao, R. Shi, L. Shang, Y.F. Zhao, G.I.N. Waterhouse, L.Z. Wu, C.H. Tung, T.R. Zhang, *ChemPlusChem* 82 (2017) 181–185.
- [7] H. Zhao, X.L. Ding, B. Zhang, Y.X. Li, C.Y. Wang, *Sci. Bull.* 62 (2017) 602–609.
- [8] M.C. Liu, L.Z. Wang, G.M. Lu, X.D. Yao, L.J. Guo, *Energy Environ. Sci.* 4 (2011) 1372–1378.
- [9] K. Iwashina, A. Kudo, *J. Am. Chem. Soc.* 34 (2011) 13272–13275.
- [10] M.N. Garica, P. Verma, Y. Kuwahara, T. Kamegawa, K. Mori, H. Yamashita, *J. Photochem. Photobiol. A Chem.* 358 (2018) 327–333.
- [11] E.A. Hameed, M.A. Gondal, Z.H. Yamani, *Catal. Commun.* 5 (2004) 715–719.
- [12] T.W. Kim, K.S. Choi, *Science* 10 (2016) 1–7.
- [13] R. Abe, M. Higashi, K. Domen, *J. Am. Chem. Soc.* 34 (2010) 11828–11829.
- [14] K. Maeda, K. Teramura, D. Lu, T. Takata, N. Satio, Y. Inoue, K. Domen, *Nature* 440 (2006) 295.
- [15] Z. Wang, Y. Inoue, T. Hisatomi, R. Ishikawa, Q. Wang, T. Takata, S. Chen, N. Shibata, Y. Ikuhara, K. Domen, *Nat. Catal.* 1 (2018) 756.
- [16] C.S. Pan, T. Takata, K. Domen, *Chem. Eur. J.* 22 (2016) 1854–1862.
- [17] J. Liu, Y. Liu, N.Y. Liu, Y.Z. Han, X. Zhang, H. Huang, Y. Lifshitz, S.T. Lee, J. Zhong, Z.H. Kang, *Science* 347 (2015) 970–974.
- [18] X.J. Guan, F.A. Chowdury, Y.J. Wang, N. Pant, S. Vanka, M.L. Trudeau, L.J. Guo, L. Vayssières, Z.T. Mi, *ACS Energy Lett.* 3 (2018) 2230–2231.
- [19] Y.P. Xie, Z.B. Yu, G. Liu, X.L. Ma, H.M. Cheng, *Energy Environ. Sci.* 7 (2014) 1895–1901.
- [20] B. Alotaibi, H.P.T. Nguyen, S. Zhao, M.G. Kibria, S. Fan, Z.T. Mi, *Nano Lett.* 13 (2013) 4356–4362.
- [21] K. Fujiwara, Y. Kuwahara, Y. Sumida, H. Yamashita, *Langmuir* 32 (2017) 6314–6321.
- [22] S.J. Deng, Y. Zhong, Y.X. Zeng, Y.D. Wang, Z.J. Yao, F. Yang, S.W. Lin, X.H. Lu, X.H. Xia, J.P. Tu, *Adv. Mater.* 29 (2017) 1700748.
- [23] L. Yu, H.Q. Zhou, J.Y. Sun, F. Qin, D. Luo, L.X. Xie, F. Yu, J.J. Bao, Y. Li, Y. Yu, S. Chen, Z.F. Ren, *Nano Energy* 41 (2017) 327–336.
- [24] Q. Li, J.J. Fu, W.L. Zhu, Z.Z. Chen, B. Shen, L.H. Wu, Z. Xi, T.Y. Wang, G. Lu, J.J. Zhu, S.S. Sun, *J. Am. Chem. Soc.* 139 (2017) 4290–4293.
- [25] J.D. Benck, Z.B. Chen, L.Y. Kuritzky, A.J. Forman, T.F. Jaramillo, *ACS Catal.* 2 (2012) 1916–1923.
- [26] K. Maeda, K. Teramura, T. Takata, M. Hara, N. Saito, K. Toda, Y. Inoue, H. Kobayashi, K. Domen, *J. Phys. Chem. B* 109 (2005) 20504–20510.
- [27] K. Maeda, K. Domen, *J. Phys. Chem. C* 111 (2007) 7851–7861.
- [28] K. Maeda, K. Domen, *J. Phys. Chem. Lett.* 1 (2010) 2655–2661.
- [29] K. Maeda, K. Domen, *Chem. Mater.* 22 (2010) 612–623.
- [30] X. Li, J.G. Yu, M. Jaroniec, X.B. Chen, *Chem. Rev.* 119 (2019) 3962–4179.
- [31] M.C. Liu, Y. Yang, N.X. Li, Y.C. Du, D.X. Song, L.J. Ma, Y. Wang, Y.Q. Zheng, D.W. Jing, *Appl. Phys. Lett.* 111 (2017) 073903.
- [32] T. Yodo, H. Yona, H. Ando, D. Nosei, *Appl. Phys. Lett.* 80 (2002) 967–990.
- [33] M.F. Dou, C. Persson, *Cryst. Growth Des.* 14 (2014) 4937–4943.
- [34] X.J. Guan, L.J. Guo, *ACS Catal.* 4 (2014) 3020–3026.
- [35] W.Q. Zhang, X. Zhang, L. Chen, J.Y. Dai, Y. Ding, L.F. Ji, J. Zhao, M. Yan, F.C. Yang, C.R. Chang, S.J. Guo, *ACS Catal.* 8 (2018) 8092–8099.